

On hallucinations in tomographic image reconstruction

Sayantana Bhadra*, Varun A. Kelkar*, Frank J. Brooks and Mark A. Anastasio, *Senior Member, IEEE*

Abstract—Tomographic image reconstruction is generally an ill-posed linear inverse problem. Such ill-posed inverse problems are typically regularized using prior knowledge of the sought-after object property. Recently, deep neural networks have been actively investigated for regularizing image reconstruction problems by learning a prior for the object properties from training images. However, an analysis of the prior information learned by these deep networks and their ability to generalize to data that may lie outside the training distribution is still being explored. An inaccurate prior might lead to false structures being hallucinated in the reconstructed image and that is a cause for serious concern in medical imaging. In this work, we propose to illustrate the effect of the prior imposed by a reconstruction method by decomposing the image estimate into generalized measurement and null components. The concept of a hallucination map is introduced for the general purpose of understanding the effect of the prior in regularized reconstruction methods. Numerical studies are conducted corresponding to a stylized tomographic imaging modality. The behavior of different reconstruction methods under the proposed formalism is discussed with the help of the numerical studies.

Index Terms—Tomographic image reconstruction, image quality assessment, deep learning, hallucinations

I. INTRODUCTION

IN tomographic imaging, a reconstruction method is employed to estimate the sought-after object from a collection of measurements obtained from an imaging system [1]. It is often desirable to reconstruct images from as few measurements as possible, without compromising on the diagnostic quality of the image. For example, data-acquisition times in magnetic resonance imaging (MRI) can be reduced by undersampling the k-space [2]. In such situations the acquired measurements are said to be *sparse* or *incomplete*, i.e. they are generally insufficient to uniquely specify the sought-after object even in the absence of measurement noise or errors related to modeling the imaging system. This naturally implies that the inverse problem is ill-posed and some form of regularization needs to be performed with priors imposed on the sought-after object. Various methods have been proposed for regularization

that can effectively mitigate the impact of measurement-incompleteness on image reconstruction. Among these methods, regularization using sparsity-promoting penalties has been employed widely [3]–[6].

Recently, there has been considerable focus on developing regularization strategies that seek to learn the prior distribution that describes the object to-be-imaged from existing data, instead of using hand-crafted priors such as sparsity-promoting penalties. Nascent deep learning-based methods have inspired a new wave of reconstruction methods that implicitly or explicitly learn the prior distribution from a set of training images in order to regularize the reconstruction problem [7]–[9]. However, such learning-based methods have also raised concerns regarding their robustness and their ability to generalize to measurements that may lie outside the distribution of the training data [10]–[12]. This is particularly relevant in the field of medical imaging where novel abnormalities can be present in the observed measurement data that may not be encountered even with a large training dataset. Moreover, simulation studies have shown that deep learning-based reconstruction methods are inherently unstable, i.e. small perturbations in the measurement may produce large differences in the reconstructed image [11], [12].

The potential lack of generalization of deep learning-based reconstruction methods as well as their innate unstable nature may cause false structures to appear in the reconstructed image that are absent in the object being imaged. These false structures may arise due to the reconstruction method incorrectly estimating parts of the object that either did not contribute to the observed measurement data or cannot be recovered in a stable manner, a phenomenon that can be termed as *hallucination*. The presence of such false structures in reconstructed images can possibly lead to an incorrect medical diagnosis. Hence, there is an urgent need to investigate the nature and impact of false structures arising out of hallucinations from deep learning-based reconstruction methods for tomographic imaging.

The topic of image hallucinations has previously been studied within the context of image super-resolution [13]–[16]. In image super-resolution, the term hallucination generally refers to high-frequency features that are introduced into the high-resolution image but do not exist in the measured low-resolution image. Hallucinations can also be realized in more general inverse problems such as image reconstruction. In such cases, the structure of the imaging operator null space is generally more complicated and the hallucinations may not be confined to high-frequency structures [17]. However, a formal definition of hallucinations within the context of such inverse

This work was supported in part by NIH Awards EB020604, EB023045, NS102213, EB028652, and NSF Award DMS1614305.

Sayantana Bhadra is with the Department of Computer Science and Engineering, Washington University in St. Louis, St. Louis, MO 63130 USA (e-mail: sayantanbhadra@wustl.edu).

Varun A. Kelkar is with the Department of Electrical and Computer Engineering, University of Illinois at Urbana-Champaign, Urbana, IL 61801 USA (e-mail: vak2@illinois.edu).

Frank J. Brooks and Mark A. Anastasio are with the Department of Bioengineering, University of Illinois at Urbana-Champaign, Urbana, IL 61801 USA (e-mail: fjb,maa@illinois.edu).

*Sayantana Bhadra and Varun A. Kelkar contributed equally.

problems has not been reported.

This study proposes a way to mathematically formalize the concept of hallucinations for general linear imaging systems that is consistent with both the mathematical notion of a hallucination in image super-resolution and the intuitive notion of hallucinations as “artifacts or incorrect features that occur due to the prior that cannot be produced from the measurements”. In addition, the notion of a *task-informed* or *specific* hallucination map is introduced. Through preliminary numerical studies, the behavior of different reconstruction methods under the proposed formalism is illustrated. It is shown that, in certain cases, traditional error maps are insufficient for visualizing and detecting specific hallucinations.

The remainder of this paper is organized as follows. In Sec. II, salient aspects of linear operator theory are reviewed, and the need for describing hallucinations based on the measurement and null space components is motivated. The concept of a hallucination map is introduced in Sec. III, along with a definition of specific hallucination maps. Sections IV and V describe the numerical studies performed to demonstrate the potential utility of proposed hallucination maps with a stylized tomographic imaging modality. Finally, a discussion and summary of the work is presented in Sec. VI.

II. BACKGROUND

A. Imaging models

A linear digital imaging system can be described as a continuous-to-discrete (CD) mapping [17], [18]:

$$\mathbf{g} = \mathcal{H}f(\mathbf{r}) + \mathbf{n}, \quad (1)$$

where $f(\mathbf{r}) \in \mathbb{L}_2(\mathbb{R}^d)$ is a function of continuous variables that represents the object being imaged, the vector $\mathbf{g} \in \mathbb{E}^M$ denotes the measured data samples and $\mathbf{n} \in \mathbb{E}^M$ is the measurement noise. The linear CD operator $\mathcal{H} : \mathbb{L}_2(\mathbb{R}^d) \rightarrow \mathbb{E}^M$ describes the action of the imaging system. In practice, discrete-to-discrete (DD) imaging models are often employed as approximations to the true CD imaging model. In a DD model, an N -dimensional approximation of $f(\mathbf{r})$ is utilized [17], [18]:

$$f_a(\mathbf{r}) = \sum_{n=1}^N [\theta]_n \psi_n(\mathbf{r}), \quad (2)$$

where the subscript a stands for approximate, $[\theta]_n$ is the n -th element of the coefficient vector $\boldsymbol{\theta} \in \mathbb{E}^N$ and $\psi_n(\mathbf{r})$ is the n -th expansion function. On substitution from Eq. (2) in Eq. (1), the DD imaging system can be expressed as

$$\mathbf{g} \approx \mathcal{H}f_a(\mathbf{r}) + \mathbf{n} = \sum_{n=1}^N [\theta]_n \mathcal{H}\psi_n(\mathbf{r}) + \mathbf{n} \equiv \mathbf{H}\boldsymbol{\theta} + \mathbf{n}, \quad (3)$$

where $\mathbf{H} : \mathbb{E}^N \rightarrow \mathbb{E}^M$ is the system matrix constructed using \mathcal{H} and $\{\psi_n(\mathbf{r})\}_{n=1}^N$. Image reconstruction methods based on Eq. (3) seek to estimate $\boldsymbol{\theta}$ from \mathbf{g} , after which the approximate object function $f_a(\mathbf{r})$ can be determined by use of Eq. (2). A well-known expansion function is the pixel expansion

function. For two-dimensional objects $f(\mathbf{r})$ with $\mathbf{r} = (x, y)$, the pixel expansion function can be expressed as [18]:

$$\psi_n(\mathbf{r}) = \begin{cases} 1, & \text{if } |x - x_n| \text{ and } |y - y_n| \leq \frac{\gamma}{2} \\ 0, & \text{otherwise} \end{cases} \quad (4)$$

where $\mathbf{r}_n = (x_n, y_n)$ represents the coordinates of the n -th grid point of a uniform Cartesian lattice and γ denotes the spacing between the lattice points. When a pixel expansion function is employed, the corresponding coefficient vector $\boldsymbol{\theta}$ directly provides a digital image representation of the continuous object function $f_a(\mathbf{r})$.

B. Generalized measurement and null components

For the DD imaging model described by Eq. (3), the properties of \mathbf{H} affect the ability to estimate $\boldsymbol{\theta}$ uniquely and stably. In the absence of measurement noise, if \mathbf{g} is sufficient to uniquely determine $\boldsymbol{\theta}$, \mathbf{H} is a full-rank operator that describes an injective mapping between \mathbb{E}^N and \mathbb{E}^M . However, for robustness in the presence of measurement noise, the criterion of *stability* is necessary in addition to uniqueness. Stability is a way of quantifying how “close” two estimates $\hat{\boldsymbol{\theta}}_1, \hat{\boldsymbol{\theta}}_2$ of $\boldsymbol{\theta}$ will be, if they are estimated from two “close” measurement vectors \mathbf{g}_1 and \mathbf{g}_2 respectively. For instance, \mathbf{g}_1 and \mathbf{g}_2 may correspond to the same object but differ due to them having two different measurement noise realizations. A popular notion of stability is based on how the ℓ_2 -distance between $\hat{\boldsymbol{\theta}}_1$ and $\hat{\boldsymbol{\theta}}_2$ relates to that between \mathbf{g}_1 and \mathbf{g}_2 [19]:

$$\|\hat{\boldsymbol{\theta}}_1 - \hat{\boldsymbol{\theta}}_2\|_2 \leq \alpha \|\mathbf{g}_1 - \mathbf{g}_2\|_2, \quad (5)$$

where α is a constant that depends only on \mathbf{H} .

Stability can also be analyzed through the lens of the singular value decomposition (SVD) of \mathbf{H} [17]:

$$\mathbf{H} = \sum_{n=1}^R \sqrt{\mu_n} \mathbf{v}_n \mathbf{u}_n^\dagger. \quad (6)$$

Here, \mathbf{u}_n and \mathbf{v}_n are the singular vectors of \mathbf{H} and $\sqrt{\mu_n}$ are the singular values. The vector \mathbf{u}_n^\dagger is the adjoint of \mathbf{u}_n and the integer $R > 0$ denotes the rank of \mathbf{H} . The singular values $\sqrt{\mu_n}$ are ordered such that $\mu_1 \geq \mu_2 \geq \dots \geq \mu_R > 0$.

A pseudoinverse-based estimate of $\boldsymbol{\theta}$ can be computed as $\hat{\boldsymbol{\theta}}_{pinv} \equiv \mathbf{H}^+ \mathbf{g}$, where the linear operator \mathbf{H}^+ denotes the Moore-Penrose pseudoinverse of \mathbf{H} that can be expressed as

$$\mathbf{H}^+ = \sum_{n=1}^R \frac{1}{\sqrt{\mu_n}} \mathbf{u}_n \mathbf{v}_n^\dagger. \quad (7)$$

From Eq. (3), due to the linearity of \mathbf{H}^+ , $\hat{\boldsymbol{\theta}}_{pinv}$ can be represented as

$$\hat{\boldsymbol{\theta}}_{pinv} = \mathbf{H}^+ \mathbf{g} \approx \mathbf{H}^+ (\mathbf{H}\boldsymbol{\theta} + \mathbf{n}) = \mathbf{H}^+ \mathbf{H}\boldsymbol{\theta} + \mathbf{H}^+ \mathbf{n} \quad (8)$$

Due to the presence of the term $\mathbf{H}^+ \mathbf{n}$ in Eq. (8), when the trailing singular values of \mathbf{H} are small, α in Eq. (5) is large, leading to unstable estimates of $\boldsymbol{\theta}$. In this scenario, a truncated pseudoinverse can be defined as

$$\mathbf{H}_P^+ = \sum_{n=1}^P \frac{1}{\sqrt{\mu_n}} \mathbf{u}_n \mathbf{v}_n^\dagger, \quad (9)$$

where the integer $P \leq R$ is chosen such that, for a given tolerance $\alpha = 1/\sqrt{\epsilon}$, $\mathbf{H}_P^+ \mathbf{g}$ is a stable, linear estimate of $\boldsymbol{\theta}$ according to Eq. (5) with $\mu_P > \epsilon \geq \mu_{P+1}$. The truncated pseudoinverse can be used to form projection operators that project $\boldsymbol{\theta} \in \mathbb{E}^N$ onto orthogonal subspaces – the ‘generalized’ null and measurement spaces [20]. The generalized null space of \mathbf{H} , denoted by $\mathcal{N}_P(\mathbf{H})$, is spanned by the singular vectors $\{\mathbf{u}_n\}_{n=P+1}^N$ that correspond to singular values satisfying $\sqrt{\mu_n} \leq \epsilon$. The orthogonal complement of the generalized null space is the generalized measurement space $\mathcal{N}_P^\perp(\mathbf{H})$.

Definition II.1 (*Generalized measurement and null components*). Let \mathbf{H} and \mathbf{H}_P^+ denote the forward and truncated pseudoinverse operators, described in Equations (3) and (9) respectively. The coefficient vector $\boldsymbol{\theta}$ can be uniquely decomposed as $\boldsymbol{\theta} = \boldsymbol{\theta}_{meas} + \boldsymbol{\theta}_{null}$, where $\boldsymbol{\theta}_{meas} \in \mathcal{N}_P^\perp(\mathbf{H})$ and $\boldsymbol{\theta}_{null} \in \mathcal{N}_P(\mathbf{H})$ are specified as

$$\boldsymbol{\theta}_{meas} = \mathcal{P}_{meas} \boldsymbol{\theta} = \mathbf{H}_P^+ \mathbf{H} \boldsymbol{\theta}, \quad (10)$$

and

$$\boldsymbol{\theta}_{null} = \mathcal{P}_{null} \boldsymbol{\theta} = [\mathbf{I}_N - \mathbf{H}_P^+ \mathbf{H}] \boldsymbol{\theta}. \quad (11)$$

Here, the projection operators \mathcal{P}_{meas} and \mathcal{P}_{null} project $\boldsymbol{\theta}$ to $\mathcal{N}_P^\perp(\mathbf{H})$ and $\mathcal{N}_P(\mathbf{H})$ [17], and \mathbf{I}_N is the identity operator in \mathbb{E}^N .

In special cases where the singular values $\sqrt{\mu_n}$ and the tolerance ϵ are such that $P = R$, the generalized null space is spanned by the singular vectors $\{\mathbf{u}_n\}_{n=R+1}^N$ with singular values $\sqrt{\mu_n} = 0$. In such cases, the generalized null space reduces to the true null space

$$\mathcal{N}_P(\mathbf{H}) = \mathcal{N}(\mathbf{H}) \equiv \{\boldsymbol{\theta} \in \mathbb{E}^N | \mathbf{H} \boldsymbol{\theta} = \mathbf{0}\}, \quad (12)$$

where $\mathbf{0}$ is the zero vector in \mathbb{E}^M . Correspondingly, the true measurement space is the orthogonal complement of the true null space. By definition, the true null space contains those object vectors that are mapped to the zero measurement data vector and hence are ‘invisible’ to the imaging system.

Having obtained the generalized measurement and null components of $\boldsymbol{\theta}$, the approximate object function $f_a(\mathbf{r})$ can also be decomposed into generalized measurement and null components:

$$\begin{aligned} f_a(\mathbf{r}) &= \sum_{n=1}^N [\boldsymbol{\theta}]_n \psi_n(\mathbf{r}) \\ &= \sum_{n=1}^N [\boldsymbol{\theta}_{meas}]_n \psi_n(\mathbf{r}) + \sum_{n=1}^N [\boldsymbol{\theta}_{null}]_n \psi_n(\mathbf{r}) \\ &= f_{a,meas}(\mathbf{r}) + f_{a,null}(\mathbf{r}). \end{aligned} \quad (13)$$

Note that for all $\mathbf{g}_1, \mathbf{g}_2 \in \mathbb{E}^M$, $\|\mathbf{H}_P^+ \mathbf{g}_1 - \mathbf{H}_P^+ \mathbf{g}_2\| \leq (1/\sqrt{\mu_P}) \|\mathbf{g}_1 - \mathbf{g}_2\|$, whereas for all $\boldsymbol{\sigma} \in \mathcal{N}_P(\mathbf{H})$, $\|\boldsymbol{\sigma}\| \geq \|\mathbf{H} \boldsymbol{\sigma}\| / \sqrt{\mu_{P+1}}$. Hence, for a given $\boldsymbol{\theta} \in \mathbb{E}^N$, $\boldsymbol{\theta}_{meas}$ is the component of $\boldsymbol{\theta}$ that can be stably estimated via the truncated pseudoinverse from the measurement data. Contrarily, $\boldsymbol{\theta}_{null}$ cannot be stably estimated from the measurement data alone; additional information provided through priors and regularization is needed to estimate this component. These observations will be essential to the definitions of hallucinations that are

provided later.

C. Regularization in tomographic image reconstruction

As discussed above, in order to obtain a stable estimate of $\boldsymbol{\theta}$ from incomplete and/or noisy measurements, imposition of prior knowledge about the object is generally needed. A flexible method of incorporating priors in the estimation of $\boldsymbol{\theta}$ is through the Bayesian formalism, where $\boldsymbol{\theta}$, \mathbf{g} and \mathbf{n} are treated as instances of random variables with distributions p_θ , p_g and p_n respectively [19]. It is assumed that p_θ , i.e. the distribution over all objects is known, and is called the *prior*. By Bayes’ theorem, the posterior distribution $p_{\theta|\mathbf{g}}$, given by

$$p_{\theta|\mathbf{g}}(\boldsymbol{\theta}|\mathbf{g}) = \frac{p_{g|\theta}(\mathbf{g}|\boldsymbol{\theta}) p_\theta(\boldsymbol{\theta})}{p_g(\mathbf{g})}, \quad (14)$$

characterizes the probability density over all possible values of the object given the prior and the noise model. Estimates such as the *maximum a posteriori* (MAP) estimate $\text{argmax}_{\boldsymbol{\theta}} p_{\theta|\mathbf{g}}(\boldsymbol{\theta}|\mathbf{g})$ can then be obtained from the posterior.

Regularization via penalization is an alternative formalism to incorporate prior knowledge. Here, the image reconstruction task is formulated as an optimization problem such as [18]

$$\hat{\boldsymbol{\theta}} = \underset{\boldsymbol{\theta}}{\text{argmin}} C_d(\mathbf{g}, \mathbf{H} \boldsymbol{\theta}) + \lambda C_p(\boldsymbol{\theta}), \quad (15)$$

where the data fidelity term $C_d(\mathbf{g}, \mathbf{H} \boldsymbol{\theta})$ enforces the estimate $\hat{\boldsymbol{\theta}}$ when acted upon by \mathbf{H} to agree with the observed measurement data \mathbf{g} and the penalty term $C_p(\boldsymbol{\theta})$ encourages the solution to be consistent with the assumed prior. The hyperparameter λ controls the trade-off between data fidelity and regularization. Often, the penalty term $R(\boldsymbol{\theta})$ is hand-crafted to encode priors such as the smoothness of natural images or sparsity of natural images in some transform domain [9]. The solution obtained through this formalism can be interpreted as the MAP estimate obtained from the Bayesian formalism in Eq. (14), with $p_\theta(\boldsymbol{\theta}) = \exp(-\lambda C_p(\boldsymbol{\theta}))$ and $p_{g|\theta}(\mathbf{g}|\boldsymbol{\theta}) = \exp(-C_d(\mathbf{g}, \mathbf{H} \boldsymbol{\theta}))$.

Regularization can also be interpreted as restricting the possible solutions to a subset $S_\mu \subset \mathbb{E}^N$, with S_μ being a member of a family of subsets parameterized by μ . The reconstruction procedure can then be represented by a possibly nonlinear mapping $\mathcal{R}_\mu : \mathbb{E}^M \rightarrow S_\mu$, with the image estimate given by $\hat{\boldsymbol{\theta}} = \mathcal{R}_\mu(\mathbf{g})$. Ideally, it is desirable that \mathcal{R}_μ satisfies the stability criterion described in Eq. (5).

Recently, methods that implicitly learn a regularizer from existing data have been proposed. Methods based on dictionary learning and learning sparsifying transforms were some of the earliest applications of such data-driven regularization [22]–[25]. However, the most actively investigated data-driven regularization methods involve learning from training data by use of deep neural networks, popularly known as deep learning [7], [26]. There have been different ways in which deep learning has been applied in the image reconstruction setting with impressive results in terms of traditional image quality metrics. A comprehensive survey of the current state of deep learning-based methods in tomographic image reconstruction can be found in recent reviews, [9], [27], [28].

However, there have been growing concerns regarding the ability of data-driven and learning based reconstruction meth-

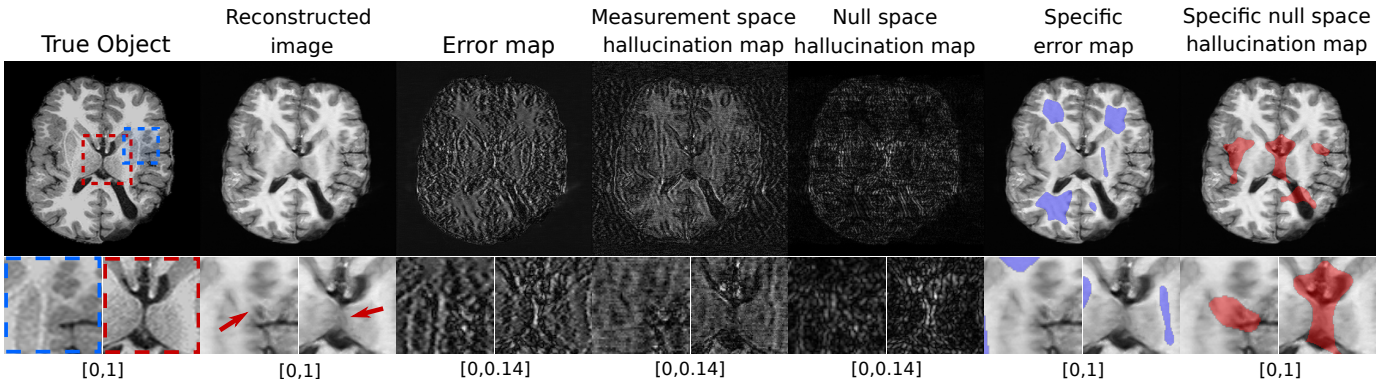


Fig. 1: Example of a true object and a U-Net based image estimate along with total error map, measurement space hallucination map, the null space hallucination map and the specific error and null space hallucination maps. The true object is outside the training data distribution of the U-Net. The regions identified by the specific null space hallucination map have lower structural similarity [21] with corresponding regions in the true image (SSIM = 0.75), compared to background regions (SSIM = 0.82).

ods to generalize to measurements that lie outside the training distribution [10]–[12], [29]. Moreover, deep learning-based reconstruction methods have been shown to not be uniformly stable, in the sense that certain imperceptible perturbations in the measurements may lead to large fluctuations in the reconstructed estimate [11], [12]. Such phenomena may lead to false structures appearing in the reconstructed image that do not exist in the object being imaged, and cannot be recovered stably from the original measurement data.

III. DEFINITION OF HALLUCINATION MAPS

When comparing or evaluating image reconstruction methods, it may be useful to visualize and quantify false structures that the methods produce and that cannot be stably recovered from the measurements. Conceptually, based on Sec. II, decomposing an object estimate into its measurement and null components is a natural first step in achieving that. As shown in Fig. 1, the difference between the reconstructed image and the true object, i.e. the *error map*, may not always be helpful in clearly identifying localized structures hallucinated by the reconstruction method, whereas decomposition into the measurement and null components may provide more insights into the nature of such false structures. In this particular example, it can be seen that although the error map shows the overall errors, localized hallucinations are better seen once the true object and its reconstructed estimate have been decomposed into the measurement and null components. There are no established methods for defining such false structures from the perspective of the generalized measurement space and null space of the imaging operator.

In order to visualize and quantify hallucinations in tomographic images, measurement and null space hallucination maps are formally defined below. The proposed definitions are general, and can be applied to any given imaging system and reconstruction method. It should be noted that the hallucinations revealed by hallucination maps should be distinguished from other artifacts that can arise in the context of tomographic imaging. Artifacts in images encompass a broad range of deviations that can appear in a reconstructed image with respect to its depiction of the object function being imaged. For example, incorrect modeling of the system matrix \mathbf{H} or

measurement noise can lead to artifacts. On the other hand, hallucinations represent incorrect features introduced by the implicit or explicit prior that cannot be stably recovered from the measurement data. The definition of hallucination maps with respect to the generalized measurement space and the null space are presented below.

A. Hallucination map in the generalized measurement space

Let $\hat{\theta}$ denote the estimate of the coefficient vector θ obtained from \mathbf{g} by use of an image reconstruction method. It is desirable that the projection of $\hat{\theta}$ onto the generalized measurement space $\mathcal{N}_P^\perp(\mathbf{H})$, i.e. $\hat{\theta}_{meas}$, should be near the truncated pseudoinverse solution $\hat{\theta}_{tp} \equiv \mathbf{H}_P^+ \mathbf{g}$. This would ensure that $\hat{\theta}_{meas}$ is consistent with the estimate of θ that can be stably recovered from \mathbf{g} . However, due to the imposed regularization in a reconstruction method, there may be discrepancies in $\hat{\theta}_{meas}$ with respect to the stable estimate $\hat{\theta}_{tp}$ in the generalized measurement space $\mathcal{N}_P^\perp(\mathbf{H})$. In order to quantify such differences, a hallucination map in the generalized measurement space is defined as follows.

Definition III.1 (*Generalized measurement space hallucination map*). As previously defined, let $\hat{\theta}$ be an image estimate obtained using a reconstruction method, and $\hat{\theta}_{tp}$ be the truncated pseudoinverse solution. The hallucination map in the measurement space is defined as,

$$\hat{\theta}_{meas}^{HM} \equiv \hat{\theta}_{meas} - \hat{\theta}_{tp}. \quad (16)$$

It should be noted that the computation of the hallucination map in the generalized measurement space requires no knowledge of the true object and simply reveals errors in the measurement component of $\hat{\theta}$ with respect to the stably computed estimate $\hat{\theta}_{tp}$.

For use in cases where pixel expansion functions are not employed, it is useful to extend the definition of hallucination maps to the object space $\mathbb{L}_2(\mathbb{R}^d)$. By use of Eq. (2), the estimate of $f_a(\mathbf{r})$ can be represented as

$$\hat{f}_a(\mathbf{r}) = \sum_{n=1}^N [\hat{\theta}]_n \psi_n(\mathbf{r}). \quad (17)$$

The hallucination map $\hat{f}_{a,meas}^{HM}(\mathbf{r})$ can be defined in the space $\mathbb{L}_2(\mathbb{R}^d)$ as

$$\hat{f}_{a,meas}^{HM}(\mathbf{r}) \equiv \sum_{n=1}^N [\hat{\theta}_{meas}^{HM}]_n \psi_n(\mathbf{r}). \quad (18)$$

B. Hallucination map in the generalized null space

As reviewed in Sec. II-B, to estimate the generalized null vector θ_{null} from \mathbf{g} , reconstruction methods that impose appropriate priors are required. Hence, to accurately capture the effect of the prior on the reconstructed image, a definition of hallucinations must satisfy the following two desiderata:

- The definition must involve the assessment of how accurate the estimate $\hat{\theta}_{null} = \mathcal{P}_{null}\hat{\theta}$ is as compared to the true generalized null vector θ_{null} .
- Since no prior is used in obtaining $\hat{\theta}_{tp}$, the definition must ensure that $\hat{\theta}_{tp}$ does not have any null space hallucinations.

With these in mind, a hallucination map $\hat{\theta}_{null}^{HM}$ in the generalized null space $\mathcal{N}_P(\mathbf{H})$ is defined as follows.

Definition III.2 (*Generalized null space hallucination map*). Consider a pixelwise indicator function $\mathbb{1} : \mathbb{R}^N \rightarrow \mathbb{R}^N$ such that for any $\vartheta \in \mathbb{R}^N$,

$$[\mathbb{1}(\vartheta)]_n = \begin{cases} 1, & \text{if } [\vartheta]_n \neq 0 \\ 0, & \text{if } [\vartheta]_n = 0. \end{cases} \quad (19)$$

Then, the hallucination map $\theta_{null}^{HM} \in \mathbb{E}^N$ can be defined as

$$\theta_{null}^{HM} \equiv \mathbb{1}(\hat{\theta}_{null}) \odot (\hat{\theta}_{null} - \theta_{null}), \quad (20)$$

where \odot denotes the Hadamard product or element-wise multiplication. Note that the indicator function in the definition ensures that $\hat{\theta}_{tp}$ does not possess any null space hallucinations, since it has no incorrect features introduced by the prior.

It is important to highlight that, for the computation of the hallucination map in the generalized null space, one must have full knowledge of the generalized null component of the true object. This is in contrast to the hallucinations in the generalized measurement space, where the knowledge of the generalized measurement component of the true object is not required. This simply reflects that, according to the provided definitions, the generalized null space hallucination maps depict errors in the reconstructed null component of the object, while the generalized measurement space hallucination maps depict errors in the component of the object that can be stably reconstructed via a truncated pseudoinverse operator from the observed measurement data.

This difference in the two definitions is associated with the fact that $\hat{\theta}_{tp}$ is close to $\mathbf{H}_P^+ \mathbf{H} \theta$ if the measurement noise is small in the sense of Eq. (5). Hence, the proposed definition of θ_{meas}^{HM} is able to reveal the effect of the prior on the reconstructed generalized measurement space component, without requiring the ground truth. In this sense, there is no analog of a stably reconstructed component like $\hat{\theta}_{tp}$ in the null space; hence invoking the true null component is necessary for defining θ_{null}^{HM} . Note that due to our definition, $\hat{\theta}_{meas}^{HM}$ may also

be influenced by the different noise propagation characteristics of the methods employed to form $\hat{\theta}_{tp}$ and $\hat{\theta}$ and therefore may not solely quantify errors associated with the prior.

It should also be noted that the errors introduced by the prior in the measurement space can be remedied by adopting a reconstruction method that penalizes measurement space hallucinations without any prior knowledge of the object, e.g., via a data consistency constraint [12] or null space shuttle procedure [20]. Accordingly, for such constrained image reconstruction methods, analyzing hallucinations in the null space is critical towards understanding the effect of the prior on the image estimate.

Similar to the hallucination map in the generalized measurement space, the hallucination map $\hat{f}_{a,null}^{HM}(\mathbf{r})$ can be defined in the space $\mathbb{L}_2(\mathbb{R}^d)$ as

$$\hat{f}_{a,null}^{HM}(\mathbf{r}) \equiv \sum_{n=1}^N [\hat{\theta}_{null}^{HM}]_n \psi_n(\mathbf{r}). \quad (21)$$

According to the proposed definitions, the truncated pseudoinverse solution $\hat{\theta}_{tp}$ has zero hallucination in both the generalized measurement space and null space. However, that does not necessarily imply that $\hat{\theta}_{tp}$ is without artifacts, since $\hat{\theta}_{tp}$ ignores θ_{null} completely. The computation of $\hat{\theta}_{tp}$ leads to the recovery of only θ_{meas} that can be estimated stably. When other regularized reconstruction methods attempt to reduce artifacts by imposing priors to estimate θ_{null} , a trade-off is made between the estimation of θ_{meas} and θ_{null} that can potentially lead to hallucinations in the generalized measurement space and null space.

C. Specific hallucination maps

The use of objective, or task-based, measures of image quality for evaluating imaging systems has been widely advocated [17]. However, the hallucination maps as defined in Section III do not incorporate any task-specific information. In particular, $\hat{\theta}_{null}^{HM}$ may contain an abundance of structures or textures, some of which may not confound an observer on a specified diagnostic task. Hence, it may be useful to identify those structures or textures in the hallucination maps that are task-relevant. One possible way to accomplish this is to process the hallucination map via an image processing transformation T , such that potentially task-relevant features or textures are localized while others are suppressed [30], [31]. Formally, this can be described as:

$$\hat{\theta}_{null}^{SHM} = T \hat{\theta}_{null}^{HM}, \quad (22)$$

where the processed pixel map $\hat{\theta}_{null}^{SHM}$ that preserves task-specific information is referred to as a *specific hallucination map*. Note that the design of the transformation T is application-dependent, as it should localize those structures or textures from the hallucination map that are relevant to a specified task. Moreover, the specification of observer (which could be a human or computational procedure) who will perform the task should also influence the design of T , as the extent to which hallucinations impact observer performance will vary. While requiring significant effort to formulate, specific hallucination maps open up the possibility of comparing

reconstruction methods based on their propensities for creating hallucinations that influence task-performance.

IV. NUMERICAL STUDIES

Numerical studies were conducted to demonstrate the utility of the proposed hallucination maps. Although the focus of these preliminary studies is on null space hallucination maps, the presented analyses could readily be repeated by use of measurement space hallucination maps. Hallucination maps were employed to reveal how data-driven reconstruction methods can behave differently on in-distribution and out of distribution images, while conventional model-based methods that employ hand-crafted priors do not.

A. Stylized imaging system

A stylized two-dimensional (2D) single-coil magnetic resonance (MR) imaging system was considered. Because physical factors such as the existence of phase shift was not considered, it should be noted that the assumed imaging operator was not intended to accurately model a real-world MR imager. Instead, the purpose of the presented simulation studies is only to demonstrate the potential utility of hallucination maps.

Fully-sampled k-space data were emulated by applying the 2D Fast Fourier Transform (FFT) on the digital objects described below. Independent and identically distributed Gaussian noise was added to the complex-valued k-space data [32]. A uniform Cartesian undersampling mask with an undersampling factor of 3 was applied on the fully-sampled k-space data to obtain undersampled measurements, as shown in Fig. S.1 in the Supplementary file. The k-space lines that were not sampled were subsequently zero-filled. The Moore-Penrose pseudoinverse \mathbf{H}^+ was applied by performing the inverse 2D Fast Fourier Transform (IFFT) on the zero-filled k-space data. Since the true pseudoinverse was considered without any truncation of singular values, the hallucination map in the generalized null space in our studies corresponds to the hallucination map in the true null space.

B. Reconstruction methods

Both data-driven and non-data-driven image reconstruction methods were investigated. The data-driven method considered was a U-Net based method [33]–[35], which learns a mapping from an initial image estimate that contains artifacts due to undersampling to the ground truth images. Two different non-data-driven reconstruction methods were considered. The first method, which is known as penalized least-squares with total variation (PLS-TV) [6], involves solving a least-squares optimization problem with a total variation penalty [6]. The second method is known as the deep image prior (DIP) [36], [37], where the reconstructed estimate is constrained to lie in the range of an untrained deep network [26] such that the estimate agrees with the observed measurements in a least-squares sense. These reconstruction methods are described in detail in Sec. S.I of the Supplementary file.

C. Training, validation and test data

For the U-Net based reconstruction method, training was performed on 2D axial adult brain MRI images from the NYU fastMRI Initiative database [38]. These will be referred to as the in-distribution (IND) images. The training and validation datasets contained 2500 and 500 images, respectively. For testing, both IND and out-of-distribution (OOD) images were considered. The OOD images were obtained from a pediatric epilepsy resection MRI dataset [39]. Both the IND and OOD testing datasets contained 69 images. It should be noted that the OOD images differed from the IND images in several aspects, such as the nature of the objects (adult for IND and pediatric for OOD) as well as the use of different MR systems used to obtain the ground truth images in each case. All images were of dimension 320×320 .

After creating the training, validation and test datasets, neural network training was performed with the IND training and validation datasets for the U-Net method. At test time, images were reconstructed from both IND and OOD test datasets using the U-Net, PLS-TV and DIP methods. Details regarding the implementation of these methods are presented in Sec. S.II of the Supplementary file.

D. Computation of hallucination maps

After images were reconstructed from the testing data, null space hallucination maps $\hat{\theta}_{null}^{HM}$ were computed. The quantities $\hat{\theta}_{null}$ and θ_{null} , as required by Eq. (20), were computed according to Eq. (11). Subsequently, specific null space hallucination maps $\hat{\theta}_{null}^{SHM}$ were also computed. In this preliminary study, these maps were designed for the purpose of localizing regions where coherent structures, as opposed to random errors, were present in $\hat{\theta}_{null}^{HM}$. Such structured hallucinations could be relevant to certain signal detection tasks. To accomplish this, the transformation T in Eq. (22) was implemented as follows. First, the region of support of each object was identified using Otsu’s method [40] and binary support masks were formed for each object. The support masks were applied on the $\hat{\theta}_{null}^{HM}$ such that errors in the reconstructed image that lie outside the region of support could be ignored. Subsequently, histogram equalization was performed. A 2D Gaussian filter with kernel width of 7 was applied on the histogram-equalized map in order to obtain a smooth distribution of intensities across the hallucination map. The width of the Gaussian filter was chosen heuristically in this study. Finally, a binary threshold was applied where the cut-off value was set to the 95-th percentile of intensity values in the processed map, such that intensities below the threshold were set to zero and intensities above the threshold were set to 1. From the thresholded maps, connected components that had a size of less than 100 pixels ($\approx 0.1\%$ of total number of pixels in each image) were eliminated to remove localized regions with negligible dimensions, resulting in the specific hallucination maps $\hat{\theta}_{null}^{SHM}$ for our studies. This procedure for computing the action of T was repeated for all $\hat{\theta}_{null}^{HM}$ computed from both the IND and OOD test datasets for each reconstruction method. It should be noted that this procedure serves only as a simplistic example of the computation of a

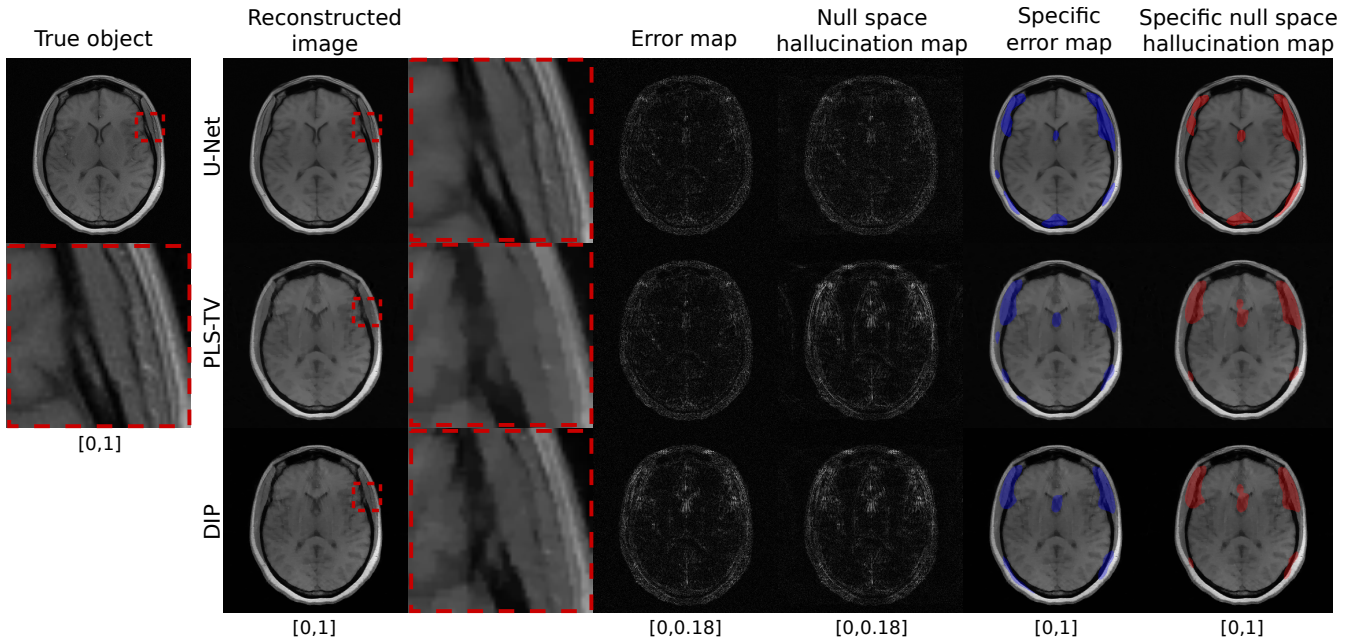


Fig. 2: Example of a ground truth and reconstructed images along with error maps and hallucination maps (null space) for IND data with different reconstruction methods – U-Net (top), PLS-TV (middle) and DIP (bottom). Expanded regions are shown to the right of the reconstructed images. The U-Net based reconstruction has fewer artifacts due to oversmoothing compared to PLS-TV and DIP, which is also reflected in its lower intensities in the error map and hallucination map. Note that for all three methods, the error maps and hallucination maps have similar characteristics.

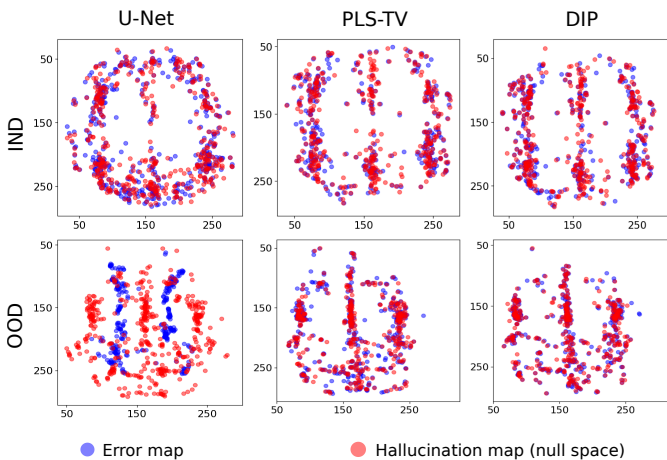


Fig. 3: Scatter plots for centroids of localized regions in specific error maps and specific null space hallucination maps with different reconstruction methods for IND (top) and OOD (bottom) data. Note that for reconstructed images with the U-Net method from OOD data, the localized regions in the specific error maps and specific hallucination maps are differently placed.

specific hallucination map, and there is no suggestion that it is optimal in any sense.

Finally, conventional error maps were computed as the difference between the reconstructed estimate $\hat{\theta}$ and the true object θ . In order to demonstrate the potential utility of the specific hallucination maps over processed versions of conventional error maps, *specific error maps* were formed by acting T on the error maps.

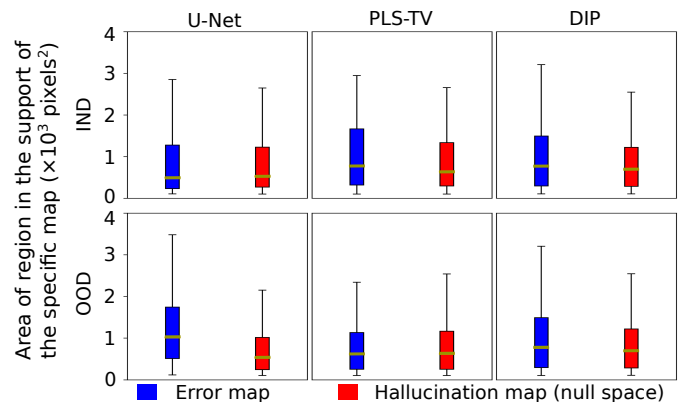


Fig. 4: Box plots of areas occupied by localized regions in specific error maps and specific null space hallucination maps with different reconstruction methods for IND (top) and OOD (bottom) data. Note that for reconstructed images with the U-Net method from OOD data, the medians of the areas of localized regions in the respective specific maps are significantly different.

V. RESULTS

The numerical results are organized as follows. First, the impact of the implicit data-driven prior in the U-Net method as characterized by differences between specific error maps and specific null space hallucination maps from OOD data are presented. This is followed by a demonstration of the difference in the performance of U-Net method between IND and OOD data as measured relative to the non-data driven methods in our studies – PLS-TV and DIP.

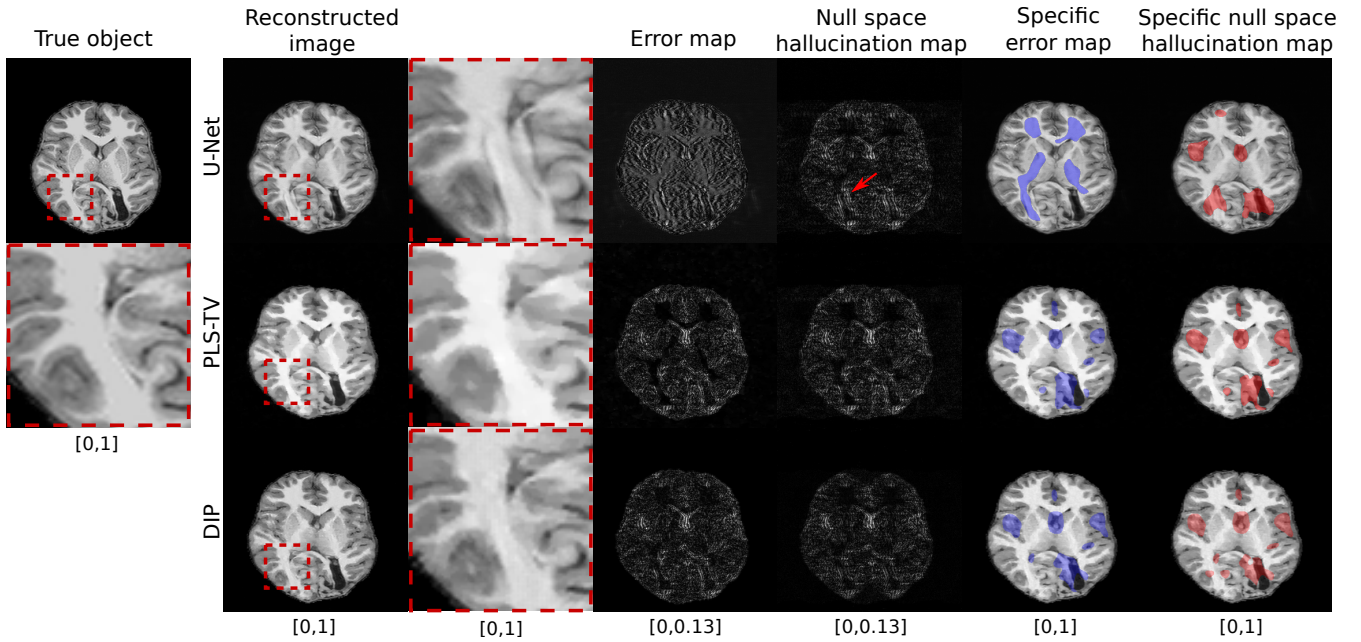


Fig. 5: Example of ground truth and reconstructed images along with error map and hallucination map (null space) for OOD data with different reconstruction methods – U-Net (top), PLS-TV (middle) and DIP (bottom). Expanded regions are shown to the right of the reconstructed images, where the U-Net method displays some distinct artifacts. It can be observed that the error map and null space hallucination map have significantly different characteristics for the U-Net method, but they are similar for PLS-TV and DIP.

A. Differences between error and hallucination maps

Reconstructed images with corresponding error maps and null space hallucination maps from an IND measurement are shown in Fig. 2. As expected, the U-Net method performs well, leading to mostly low intensity regions in the error map and the null space hallucination map. Furthermore, the error map appears visually similar to the null space hallucination map (both original and specific), suggesting that the error in the measurement component is small. Since the PLS-TV and DIP methods promote data fidelity and generalization error is not an issue, the respective error map and hallucination map appear to be similar as well.

To further demonstrate that the specific hallucination and specific error maps convey similar information for this IND study, scatter plots of the centroids of the detected regions in each type of map corresponding to the ensemble of IND reconstructed images from all three reconstruction methods are shown in Fig. 3 (top row). From these scatter plots, it can be observed that the detected regions in the specific error maps and specific hallucination maps are centered in almost similar locations for all three reconstruction methods. Thus, in terms of expressing where error due to an inaccurate prior is likely to be localized for methods such as PLS-TV and DIP that promote data fidelity, as well as data-driven methods such as the U-Net with IND data, the specific error map and the specific null space hallucination map provide similar information. Furthermore, the areas occupied by the respective detected regions in the specific maps for all three reconstruction methods can be observed in the box plots shown in Fig. 4 (top row). The medians of areas in the detected regions in the specific error map and specific hallucination map are similar

for all three reconstruction methods, suggesting further that specific error maps and specific null space hallucination maps carry similar information in such cases.

As the distribution shifts to OOD, as shown in Fig. 5, differences begin to appear between the error map and null space hallucination map for images reconstructed by use of the U-Net method. The intensities in the error map for U-Net image are higher compared to the corresponding PLS-TV and DIP images, and distributed across the image at the same rate. The higher error for the U-Net method is a result of the change of distribution and the method’s inability to generalize well to data that are significantly out of distribution with respect to the training data. The change of distribution results in significant inaccuracies in both the measurement and null components of the reconstructed estimate produced by the U-Net and hence under such circumstances it may be difficult to localize hallucinations due to inaccuracies in the imposed prior, i.e. the null space hallucinations, just from the error map.

This is also reflected in the differences in the regions present in the specific error map and the specific hallucination map. On the other hand, for the PLS-TV and DIP methods that do not rely on training data, the characteristics between the error map and the null space hallucination map remain similar as highlighted by the respective hallucination maps. This is further validated across the ensemble of reconstructed images by observing the scatter plots of the centroids of the detected regions in the specific error maps and specific hallucination maps in Fig. 3 (bottom row). The error map centroids are generally located differently compared to the hallucination map centroids for the U-Net method. In other words, under such circumstances, one cannot rely on only the error maps without considering the corresponding hallucination maps in

order to estimate where hallucinations due to the imposed prior are likely to be localized in a reconstructed image. Moreover, the box plots in Fig. 4 show that, for the U-Net method, the median of areas in localized regions in the specific error map is appreciably higher than the median of areas in localized regions in the specific hallucination map. This suggests that there is a disagreement between the information conveyed by the error map and the null space hallucination map regarding the typical coverage of structured hallucinations in the null space due to the misinformed prior.

Thus, it can be observed that, for data-driven reconstruction methods, error maps alone may be insufficient to identify regions in the reconstructed image where hallucinations occur due to the imposed prior, and hallucination maps in the null space are required.

B. Investigation of structured hallucinations

Additional studies were conducted to validate that the specific hallucination maps actually revealed regions in the image that contain significant errors. To accomplish this, two empirical probability distribution functions (PDFs) were estimated that describe the average SSIM values computed over two non-overlapping regions in the reconstructed images for the OOD case. One region corresponded to the support of the specific hallucination maps described above and the second region was spanned by all other pixels in the image. The two empirical PDFs are shown in Fig. 6a and reveal that the mode of the distribution corresponding to the SSIM averaged over the structured hallucination regions is demonstrably lower than that describing the average SSIM values over the background regions.

The empirical PDFs that described the SSIM value averaged over the structured hallucination regions were also compared for each of the three reconstruction methods. As shown in Fig. 6b, for the IND case, the images reconstructed by use of the U-Net had significantly higher SSIM values, on average, in the structured hallucination regions as compared to both the PLS-TV and DIP methods. This can be attributed to network training with a sufficiently large amount of IND data. However, for the OOD case, as shown in Fig. 6c, the images reconstructed by use of the U-Net had similar SSIM values as those produced by the PLS-TV method, while the DIP method produced images that possessed, on average, higher SSIM values compared to the U-Net method. It should be noted that, for both the IND and OOD cases, the DIP method was implemented with the same network architecture as the U-Net based method. Thus, a shift in the data distribution for data-driven methods such as the U-Net method can manifest in structured hallucinations due to the misinformed prior that can ultimately cause significant artifacts in the reconstructed image.

VI. SUMMARY AND CONCLUSION

While regularization via sparsity-promoting penalties in an optimization-based reconstruction framework is commonly employed, emerging learning-based methods that employ deep neural networks have shown the potential to improve reconstructed image quality further by learning priors from existing data. However, an analysis of the prior information

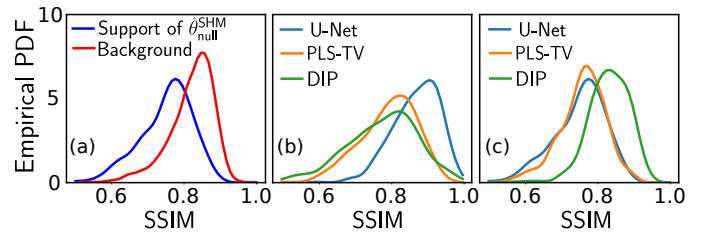


Fig. 6: (a) Empirical PDF of SSIM values in the structured hallucination regions (support of $\hat{\theta}_{null}^{SHM}$) and the regions spanned by the remaining pixels in the support of the image (background), respectively, for the U-Net method with OOD data. Empirical PDF of SSIM in the structured hallucination regions for all three reconstruction methods with (b) IND data and (c) OOD data.

learned by deep networks and their ability to generalize to data that may lie outside the training distribution is still being explored. Additionally, there are open questions and concerns about the stability of such networks when applied for image reconstruction. While it has been understood that use of an inaccurate prior might lead to false structures, or hallucinations, being introduced in the reconstructed image, formal definitions for hallucinations within the context of tomographic image reconstruction have not been reported.

In this work, by use of concepts from linear operator theory, formal definitions for hallucination maps in linear tomographic imaging problems are introduced. These provide the opportunity to isolate and visualize image hallucinations that are contained within the measurement or null spaces of a linear imaging operator. The measurement space hallucination map permits the analysis of errors in the measurement space component of a reconstructed object estimate with respect to the component of the object that can be stably computed from a given set of measurement data. Alternatively, the null space hallucination map permits analysis of errors in the null space component of a reconstructed object estimate with respect to the true object null space component. These errors are caused solely by the reconstruction prior. Both maps can be employed to systematically investigate the impact of different priors utilized in image reconstruction methods. Finally, the notion of a specific hallucination map was also introduced, which can be formulated to reveal hallucinations that are relevant to a specified image-based inference.

Numerical studies were performed with simulated under-sampled measurements from a stylized single-coil MRI system. Both data-driven and non-data-driven methods were investigated to demonstrate the utility of the proposed hallucination maps. It was observed that null space hallucination maps can be particularly useful as compared to traditional error maps when assessing the effect of data-driven priors with out-of-distribution data. Furthermore, it was shown that structured hallucinations with data-driven methods that are caused due to a shift in the data distribution may ultimately lead to significant artifacts in the reconstructed image.

The computation of the projection operations as described in Eq. (10) and Eq. (11) via the SVD may be infeasible for large-scale problems. Wilson and Barrett [41] proposed an iterative method to compute θ_{meas} and θ_{null} without explicit

computation of the SVD of \mathbf{H} . Alternatively, randomized SVD [42] is a relatively computationally efficient algorithm that can be employed to estimate these quantities. The development of computationally efficient methods for computing the projection operators for large-scale problems remains an active area of research.

There remain important topics for future investigation. Beyond the framework presented, it might be possible to derive objective figures-of-merit (FOMs) from ensembles of hallucination maps. Furthermore, the probability of occurrence of hallucinations can be potentially quantified from ensembles of hallucination maps. While understanding the interplay between hallucinations and image reconstruction priors is important in preliminary studies, ultimately, image reconstruction methods should be objectively evaluated with consideration of all physical and statistical factors.

REFERENCES

- [1] A. C. Kak, M. Slaney, and G. Wang, "Principles of computerized tomographic imaging," *Medical Physics*, vol. 29, no. 1, pp. 107–107, 2002.
- [2] A. C.-Y. Yang, M. Kretzler, S. Sudarski, V. Gulani, and N. Seiberlich, "Sparse reconstruction techniques in MRI: methods, applications, and challenges to clinical adoption," *Investigative radiology*, vol. 51, no. 6, p. 349, 2016.
- [3] D. L. Donoho, "For most large underdetermined systems of linear equations the minimal ℓ_1 -norm solution is also the sparsest solution," *Communications on Pure and Applied Mathematics: A Journal Issued by the Courant Institute of Mathematical Sciences*, vol. 59, no. 6, pp. 797–829, 2006.
- [4] D. L. Donoho and M. Elad, "Optimally sparse representation in general (nonorthogonal) dictionaries via ℓ_1 minimization," *Proceedings of the National Academy of Sciences*, vol. 100, no. 5, pp. 2197–2202, 2003.
- [5] E. J. Candes, J. K. Romberg, and T. Tao, "Stable signal recovery from incomplete and inaccurate measurements," *Communications on Pure and Applied Mathematics: A Journal Issued by the Courant Institute of Mathematical Sciences*, vol. 59, no. 8, pp. 1207–1223, 2006.
- [6] E. Y. Sidky and X. Pan, "Image reconstruction in circular cone-beam computed tomography by constrained, total-variation minimization," *Physics in Medicine & Biology*, vol. 53, no. 17, p. 4777, 2008.
- [7] G. Wang, "A perspective on deep imaging," *IEEE access*, vol. 4, pp. 8914–8924, 2016.
- [8] M. T. McCann, K. H. Jin, and M. Unser, "Convolutional neural networks for inverse problems in imaging: A review," *IEEE Signal Processing Magazine*, vol. 34, no. 6, pp. 85–95, 2017.
- [9] S. Ravishanker, J. C. Ye, and J. A. Fessler, "Image reconstruction: From sparsity to data-adaptive methods and machine learning," *Proceedings of the IEEE*, vol. 108, no. 1, pp. 86–109, 2019.
- [10] Y. Huang, T. Würfl, K. Breininger, L. Liu, G. Lauritsch, and A. Maier, "Some investigations on robustness of deep learning in limited angle tomography," in *International Conference on Medical Image Computing and Computer-Assisted Intervention*. Springer, 2018, pp. 145–153.
- [11] N. M. Gottschling, V. Antun, B. Adcock, and A. C. Hansen, "The troublesome kernel: why deep learning for inverse problems is typically unstable," *arXiv preprint arXiv:2001.01258*, 2020.
- [12] V. Antun, F. Renna, C. Poon, B. Adcock, and A. C. Hansen, "On instabilities of deep learning in image reconstruction and the potential costs of AI," *Proceedings of the National Academy of Sciences*, 2020.
- [13] S. Baker and T. Kanade, "Limits on super-resolution and how to break them," *IEEE Transactions on Pattern Analysis and Machine Intelligence*, vol. 24, no. 9, pp. 1167–1183, 2002.
- [14] W. Liu, D. Lin, and X. Tang, "Hallucinating faces: Tensorpatch super-resolution and coupled residue compensation," in *2005 IEEE Computer Society Conference on Computer Vision and Pattern Recognition (CVPR'05)*, vol. 2. IEEE, 2005, pp. 478–484.
- [15] N. Wang, D. Tao, X. Gao, X. Li, and J. Li, "A comprehensive survey to face hallucination," *International journal of computer vision*, vol. 106, no. 1, pp. 9–30, 2014.
- [16] A. Fawzi, H. Samulowitz, D. Turaga, and P. Frossard, "Image inpainting through neural networks hallucinations," in *2016 IEEE 12th Image, Video, and Multidimensional Signal Processing Workshop (IVMSP)*. Ieee, 2016, pp. 1–5.
- [17] H. H. Barrett and K. J. Myers, *Foundations of Image Science*. John Wiley & Sons, 2013.
- [18] M. A. Anastasio and R. W. Schoonover, "Basic principles of inverse problems for optical scientists," *digital Encyclopedia of Applied Physics*, pp. 1–24, 2003.
- [19] G. Bal, "Introduction to inverse problems," *Lecture Notes-Department of Applied Physics and Applied Mathematics, Columbia University, New York*, 2012.
- [20] M. M. Deal and G. Nolet, "Nullspace shuttles," *Geophysical Journal International*, vol. 124, no. 2, pp. 372–380, 1996.
- [21] Z. Wang, A. C. Bovik, H. R. Sheikh, and E. P. Simoncelli, "Image quality assessment: from error visibility to structural similarity," *IEEE transactions on image processing*, vol. 13, no. 4, pp. 600–612, 2004.
- [22] S. Ravishanker and Y. Bresler, "MR image reconstruction from highly undersampled k-space data by dictionary learning," *IEEE transactions on medical imaging*, vol. 30, no. 5, pp. 1028–1041, 2010.
- [23] S. Tiwari, K. Kaur, and K. Arya, "A study on dictionary learning based image reconstruction techniques for big medical data," in *Handbook of Multimedia Information Security: Techniques and Applications*. Springer, 2019, pp. 377–393.
- [24] S. Ravishanker and Y. Bresler, "Learning sparsifying transforms," *IEEE Transactions on Signal Processing*, vol. 61, no. 5, pp. 1072–1086, 2012.
- [25] —, "Data-driven learning of a union of sparsifying transforms model for blind compressed sensing," *IEEE Transactions on Computational Imaging*, vol. 2, no. 3, pp. 294–309, 2016.
- [26] I. Goodfellow, Y. Bengio, A. Courville, and Y. Bengio, *Deep learning*. MIT press Cambridge, 2016, vol. 1.
- [27] M. T. McCann and M. Unser, "Biomedical image reconstruction: From the foundations to deep neural networks," *arXiv preprint arXiv:1901.03565*, 2019.
- [28] K. Hammernik and F. Knoll, "Machine learning for image reconstruction," in *Handbook of Medical Image Computing and Computer Assisted Intervention*. Elsevier, 2020, pp. 25–64.
- [29] J. W. Stayman, J. L. Prince, and J. H. Siewerdsen, "Information propagation in prior-image-based reconstruction," in *Conference proceedings/International Conference on Image Formation in X-Ray Computed Tomography. International Conference on Image Formation in X-Ray Computed Tomography*, vol. 2012. NIH Public Access, 2012, p. 334.
- [30] G. Castellano, L. Bonilha, L. Li, and F. Cendes, "Texture analysis of medical images," *Clinical radiology*, vol. 59, no. 12, pp. 1061–1069, 2004.
- [31] C. L. Chowdhary and D. Acharjya, "Segmentation and feature extraction in medical imaging: a systematic review," *Procedia Computer Science*, vol. 167, pp. 26–36, 2020.
- [32] S. Aja-Fernández and G. Vegas-Sánchez-Ferrero, "Statistical analysis of noise in MRI," *Switzerland: Springer International Publishing*, 2016.
- [33] K. H. Jin, M. T. McCann, E. Froustey, and M. Unser, "Deep convolutional neural network for inverse problems in imaging," *IEEE Transactions on Image Processing*, vol. 26, no. 9, pp. 4509–4522, 2017.
- [34] Y. Han and J. C. Ye, "Framing U-Net via deep convolutional framelets: Application to sparse-view CT," *IEEE transactions on medical imaging*, vol. 37, no. 6, pp. 1418–1429, 2018.
- [35] C. M. Hyun, H. P. Kim, S. M. Lee, S. Lee, and J. K. Seo, "Deep learning for undersampled MRI reconstruction," *Physics in Medicine & Biology*, vol. 63, no. 13, p. 135007, 2018.
- [36] D. Ulyanov, A. Vedaldi, and V. Lempitsky, "Deep image prior," in *Proceedings of the IEEE Conference on Computer Vision and Pattern Recognition*, 2018, pp. 9446–9454.
- [37] D. Van Veen, A. Jalal, M. Soltanolkotabi, E. Price, S. Vishwanath, and A. G. Dimakis, "Compressed sensing with deep image prior and learned regularization," *arXiv preprint arXiv:1806.06438*, 2018.
- [38] J. Zbontar, F. Knoll, A. Sriram, M. J. Muckley, M. Bruno, A. Defazio, M. Parente, K. J. Geras, J. Katsnelson, H. Chandarana *et al.*, "fastMRI: An open dataset and benchmarks for accelerated MRI," *arXiv preprint arXiv:1811.08839*, 2018.
- [39] A. M. S. Maallo, E. Freud, T. T. Liu, C. Patterson, and M. Behrmann, "Effects of unilateral cortical resection of the visual cortex on bilateral human white matter," *NeuroImage*, vol. 207, p. 116345, 2020.
- [40] A. K. Jain, *Fundamentals of digital image processing*. Prentice-Hall, Inc., 1989.
- [41] D. W. Wilson and H. H. Barrett, "Decomposition of images and objects into measurement and null components," *Optics Express*, vol. 2, no. 6, pp. 254–260, 1998.
- [42] N. Halko, P.-G. Martinsson, and J. A. Tropp, "Finding structure with randomness: Probabilistic algorithms for constructing approximate matrix decompositions," *SIAM review*, vol. 53, no. 2, pp. 217–288, 2011.

On hallucinations in tomographic image reconstruction (Supplementary Material)

Sayantana Bhadra, Varun A. Kelkar, Frank J. Brooks and Mark A. Anastasio, *Senior Member, IEEE*

S. I. SAMPLING MASK

A uniform Cartesian undersampling mask was employed in our simulation studies for generating the incomplete k-space data. The full k-space data were undersampled by a factor of 3 using the uniform sampling mask shown in Fig. S. 1.

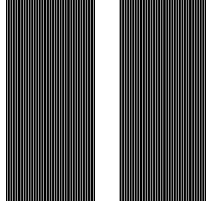


Fig. S. 1: Sampling mask

S. II. DETAILS OF RECONSTRUCTION METHODS

The details of the three reconstruction methods employed in our studies are presented below. They are based on the imaging model:

$$\mathbf{g} = \mathbf{H}\boldsymbol{\theta} + \mathbf{n}, \quad (1)$$

where $\boldsymbol{\theta} \in \mathbb{E}^N$ is the sought-after coefficient vector, $\mathbf{g} \in \mathbb{E}^M$ is the observed measurement data, $\mathbf{H} \in \mathbb{E}^{M \times N}$ is the system matrix, and $\mathbf{n} \in \mathbb{E}^N$ is iid Gaussian noise.

A. Penalized least squares with TV regularization (PLS-TV)

The PLS-TV method involves solving the penalized least-squares optimization framework with the penalty term as the TV penalty:

$$\hat{\boldsymbol{\theta}} = \underset{\boldsymbol{\theta}}{\operatorname{argmin}} \|\mathbf{g} - \mathbf{H}\boldsymbol{\theta}\|_2^2 + \lambda \|\boldsymbol{\theta}\|_{TV}, \quad (2)$$

where λ is the regularization parameter. Proximal gradient methods are commonly employed to implement the PLS-TV method [1]–[3]. In this study, PLS-TV reconstruction was performed for a dataset of measurements corresponding to 69 different images using the Berkeley Advanced Reconstruction Toolbox (BART) [4], [5]. BART performs PLS-TV reconstruction using the augmented Lagrangian based optimization method proposed in [3]. The regularization parameter λ in Eq. (2) was chosen by first performing image reconstruction on a subset of the dataset, with different values of λ . The value of λ which provided the lowest mean of the root mean squared error (RMSE) metric over the subset was chosen, and used for image reconstruction of all the images in the dataset.

B. U-Net-based reconstruction

The following procedure, known as *image-domain learning*, was employed for the U-Net based image reconstruction. First, initial estimates of the images were obtained from the measurement data by use of the pseudoinverse operator. They were then employed as inputs to a convolutional neural network (CNN), which was trained in order to produce artifact-free images, similar to images from the ground truth distribution [6]–[9]. As is common practice, the CNN architecture used in this study is the U-Net [10]. A U-Net consists of two CNNs that represent a downsampling path followed by an upsampling path respectively, and skip connections [11] between similar levels in the downsampling and upsampling paths. Let the initial estimate from the measurement data be denoted as $\boldsymbol{\theta}'$ and the function computed by the U-Net be represented as $B(\boldsymbol{\theta}'; w)$ where $B : \mathbb{E}^N \rightarrow \mathbb{E}^N$ and w denotes the weight parameters of the U-Net. Given a training data set of initial estimate-ground truth pairs $\{\boldsymbol{\theta}'_i, \boldsymbol{\theta}_i\}_{i=1}^D$ where D is the size of the training data set, the optimal weight parameters w^* are learned by approximately solving the following optimization problem:

$$w^* = \underset{w}{\operatorname{argmin}} \sum_{i=1}^D \mathcal{L}(B(\boldsymbol{\theta}'_i, w), \boldsymbol{\theta}_i), \quad (3)$$

where $\mathcal{L}(\cdot, \cdot)$ is a suitable loss function. In this work, mean absolute error was used as the loss function [12]. The model for the U-Net was based on the single-coil baseline U-Net architecture provided in [13]. A stochastic gradient-based method known as RMSProp [14] was employed to solve the optimization problem in Eq. (3). After this iterative scheme for training the U-Net reached convergence, the trained U-Net was used to reconstruct images from a previously unseen test measurement dataset, where an initial estimate $\boldsymbol{\theta}'_{test}$ computed from a test measurement data was employed to obtain the reconstructed image $\hat{\boldsymbol{\theta}}_{test} = B(\boldsymbol{\theta}'_{test}, w)$. The training and testing of the U-Net based reconstruction was performed using code available at <https://github.com/facebookresearch/fastMRI>, which utilizes PyTorch Lightning [15].

C. Deep image prior (DIP)

Recently, Ulyanov *et al.* [16] showed that a CNN $G : \mathbb{R}^k \rightarrow \mathbb{E}^N$ with randomly initialized weights w and random input $\mathbf{z} \in \mathbb{R}^k$ can be an effective regularizer for image restoration problems such as denoising, super-resolution and

inpainting. This method of regularization, known as deep image prior (DIP), utilizes the observation that the structure of deep convolutional networks captures several low-level image statistics and is biased towards smooth, natural images. Van Veen *et al.* [17] extended the DIP framework to applications in tomographic imaging from incomplete measurements with encouraging results. Essentially, image reconstruction using the DIP method can be formulated in terms of the following optimization problem:

$$\begin{aligned} w^* &= \operatorname{argmin}_w \|\mathbf{g} - \mathbf{H}G(\mathbf{z}; w)\|_2^2, \\ \hat{\boldsymbol{\theta}} &= G(\mathbf{z}; w^*) \end{aligned} \quad (4)$$

where \mathbf{z} and w are randomly initialized.

It has been shown in [16], [17] that the DIP method overfits the measurement noise upon convergence. Hence, further regularization may be required, either in the form of early stopping or with the addition of penalties in the optimization problem in Eq. (4). Inspired by [18], in our experiments, image reconstruction using the DIP method with TV regularization (DIP-TV) was performed by approximately solving the following optimization problem:

$$\begin{aligned} w^* &= \operatorname{argmin}_w \|\mathbf{g} - \mathbf{H}G(\mathbf{z}, w)\|_2^2 + \lambda \|G(\mathbf{z}, w)\|_{\text{TV}}, \\ \hat{\boldsymbol{\theta}} &= G(\mathbf{z}; w^*) \end{aligned} \quad (5)$$

where \mathbf{z} and w were randomly initialized, and λ is the regularization parameter. The same U-Net architecture employed for the U-Net based reconstruction was employed for DIP-TV, and was implemented in TensorFlow [19]. Similar to the implementation of the PLS-TV method as outlined in Sec. S. II-A, the regularization parameter λ for the TV penalty in Eq. (5) was chosen by first performing image reconstruction on a subset of the dataset, with different values of λ . Subsequently, the value which provided the lowest mean RMSE over the subset was chosen to perform image reconstruction from all the measurements. The optimization problem in Eq. (5) was approximately solved using a stochastic gradient algorithm called Adam [20].

REFERENCES

- [1] A. Chambolle, "An algorithm for total variation minimization and applications," *Journal of Mathematical Imaging and Vision*, vol. 20, no. 1-2, pp. 89–97, 2004.
- [2] A. Beck and M. Teboulle, "Fast gradient-based algorithms for constrained total variation image denoising and deblurring problems," *IEEE Transactions on Image Processing*, vol. 18, no. 11, pp. 2419–2434, 2009.
- [3] M. V. Afonso, J. M. Bioucas-Dias, and M. A. Figueiredo, "An augmented lagrangian approach to the constrained optimization formulation of imaging inverse problems," *IEEE Transactions on Image Processing*, vol. 20, no. 3, pp. 681–695, 2010.
- [4] M. Uecker, F. Ong, J. I. Tamir, D. Bahri, P. Virtue, J. Y. Cheng, T. Zhang, and M. Lustig, "Berkeley advanced reconstruction toolbox," in *Proc. Intl. Soc. Mag. Reson. Med.*, vol. 23, no. 2486, 2015.
- [5] M. U. *et al.*, "Bart toolbox for computational magnetic resonance imaging, doi: 10.5281/zenodo.592960," 2015. [Online]. Available: <http://mrirecon.github.io/bart/>
- [6] K. H. Jin, M. T. McCann, E. Froustey, and M. Unser, "Deep convolutional neural network for inverse problems in imaging," *IEEE Transactions on Image Processing*, vol. 26, no. 9, pp. 4509–4522, 2017.
- [7] Y. Han and J. C. Ye, "Framing U-Net via deep convolutional framelets: Application to sparse-view CT," *IEEE transactions on medical imaging*, vol. 37, no. 6, pp. 1418–1429, 2018.
- [8] C. M. Hyun, H. P. Kim, S. M. Lee, S. Lee, and J. K. Seo, "Deep learning for undersampled MRI reconstruction," *Physics in Medicine & Biology*, vol. 63, no. 13, p. 135007, 2018.
- [9] S. Antholzer, M. Haltmeier, and J. Schwab, "Deep learning for photoacoustic tomography from sparse data," *Inverse problems in science and engineering*, vol. 27, no. 7, pp. 987–1005, 2019.
- [10] O. Ronneberger, P. Fischer, and T. Brox, "U-Net: Convolutional networks for biomedical image segmentation," in *Medical Image Computing and Computer-Assisted Intervention – MICCAI 2015*, N. Navab, J. Hornegger, W. M. Wells, and A. F. Frangi, Eds. Cham: Springer International Publishing, 2015, pp. 234–241.
- [11] M. Drozdal, E. Vorontsov, G. Chartrand, S. Kadoury, and C. Pal, "The importance of skip connections in biomedical image segmentation," in *Deep Learning and Data Labeling for Medical Applications*. Springer, 2016, pp. 179–187.
- [12] H. Zhao, O. Gallo, I. Frosio, and J. Kautz, "Loss functions for image restoration with neural networks," *IEEE Transactions on computational imaging*, vol. 3, no. 1, pp. 47–57, 2016.
- [13] J. Zbontar, F. Knoll, A. Sriram, M. J. Muckley, M. Bruno, A. Defazio, M. Parente, K. J. Geras, J. Katsnelson, H. Chandarana *et al.*, "fastMRI: An open dataset and benchmarks for accelerated MRI," *arXiv preprint arXiv:1811.08839*, 2018.
- [14] T. Tieleman and G. Hinton, "Lecture 6.5—RMSProp: Divide the gradient by a running average of its recent magnitude," COURSE: Neural Networks for Machine Learning, 2012.
- [15] W. Falcon, "Pytorch lightning," *GitHub*. Note: <https://github.com/PyTorchLightning/pytorch-lightning> Cited by, vol. 3, 2019.
- [16] D. Ulyanov, A. Vedaldi, and V. Lempitsky, "Deep image prior," in *Proceedings of the IEEE Conference on Computer Vision and Pattern Recognition*, 2018, pp. 9446–9454.
- [17] D. Van Veen, A. Jalal, M. Soltanolkotabi, E. Price, S. Vishwanath, and A. G. Dimakis, "Compressed sensing with deep image prior and learned regularization," *arXiv preprint arXiv:1806.06438*, 2018.
- [18] J. Liu, Y. Sun, X. Xu, and U. S. Kamilov, "Image restoration using total variation regularized deep image prior," in *ICASSP 2019-2019 IEEE International Conference on Acoustics, Speech and Signal Processing (ICASSP)*. IEEE, 2019, pp. 7715–7719.
- [19] M. Abadi, P. Barham, J. Chen, Z. Chen, A. Davis, J. Dean, M. Devin, S. Ghemawat, G. Irving, M. Isard *et al.*, "Tensorflow: a system for large-scale machine learning," in *OSDI*, vol. 16, 2016, pp. 265–283.
- [20] D. P. Kingma and J. Ba, "Adam: A method for stochastic optimization," *arXiv preprint arXiv:1412.6980*, 2014.